Asymmetric Bipolar Resistive Switching of Halide Perovskite Film in Contact with TiO_2 layer

*Seongha Lee,[1] Sarah Wolfe,[1] Jorge Torres,[2] Minhee Yun,[2] Jung-Kun Lee[1,] **

[1] Department of Mechanical Engineering & Materials Science, University of Pittsburgh, Pennsylvania 15261, USA.

[2] Department of Electrical and Computer Engineering, University of Pittsburgh, Pennsylvania 15261, USA.

KEYWORDS: halide perovskite, interface, resistive switching, Schottky barrier, defects migration, asymmetry, ReRAM

ABSTRACT: Halide perovskite materials such as methylammonium lead iodide ($CH_3NH_3PbI_3$) have attracted considerable interest for the resistive random-access memory (ReRAM) applications which exploits a dramatic change in the resistance by external electric bias. In many semiconductor films, the drift, accumulation, and chain formation of defects explain the change in the resistance by external bias. This study demonstrates that the interface of $CH_3NH_3PbI_3$ with TiO_2 has a significant impact on the formation and rupture of defect chains and causes the

asymmetric bipolar resistive switching in the Au/$CH_3NH_3PbI_3$/TiO_2/FTO device. When negative bias is applied to the Au electrode, iodine interstitials with the lowest migration activation energy moves toward TiO_2 in $CH_3NH_3PbI_3$ layer and pile up at the $CH_3NH_3PbI_3$-TiO_2 interface. Under the same condition, oxygen vacancies in TiO_2 layer also travel to the $CH_3NH_3PbI_3$-TiO_2 interface and strongly attract iodine interstitials. As a result, Schottky barrier appears at the $CH_3NH_3PbI_3$-TiO_2 interface and the resistance of Au/$CH_3NH_3PbI_3$/TiO_2/FTO becomes much larger than that of Au/$CH_3NH_3PbI_3$/FTO in the high resistance state. Frequency dependence of the capacitance confirms the asymmetric appearance of large space charge polarization at the $CH_3NH_3PbI_3$-TiO_2 interface, which causes the unique bipolar resistive switching behavior with the on/off ratio (10^3) and retention time (> 10^4 seconds) at – 0.85V in Au/$CH_3NH_3PbI_3$/TiO_2/FTO film.

Introduction

The resistive random-access memory (ReRAM) devices have been developed as promising next-generation nonvolatile memory devices in future memory technology due to its simple device architecture, fast operation, and low power consumption.[1-3] To read, write and store data in a same device, ReRAMs use semiconductor or dielectric materials which show hysteresis in current – voltage relation. The resistive switching mechanism is explained by the conductive filament formation of ions and defects,[4,5] and the electrochemical reaction at the interface.[6,7] The ReRAM device has a sandwich structure which is composed of a dielectric layer and two neighbor conducting layers. The switching of resistance is observed in several types of materials including group IV and III-V semiconductors, organic compounds and inorganic materials, but the non-volatile behavior is found mainly in the binary metal oxides.[8-10]

Recently, organic-inorganic hybrid perovskite materials such as methylammonium lead iodide ($CH_3NH_3PbI_3$) have attracted intense interest from scientists and engineers due to the intriguing properties such as high absorption coefficient, convenient bandgap tunability, and long diffusion length of charge carriers.[11-13] These unique materials properties have a potential to build new photovoltaics (PVs),[14-16] light-emitting diodes (LEDs),[17-19] field effect transistor (FETs),[20] radiation detectors,[21] and lasers.[22] Furthermore, certain defects of hybrid perovskite materials, which have a low formation energy, have been also explored. Defects migration and charge trapping in the hybrid perovskite film have a negative impact on the carrier extraction phenomenon and power conversion efficiency of PVs and LEDs.[23,24]

However, the defect drift or migration in the hybrid perovskite materials can be positively utilized to design a novel memory device.[25-31] Because of these mobile ions and defects, I-V curve of the hybrid perovskite film exhibits hysteresis which enables ReRAM devices. Mixed halide perovskites such as $CH_3NH_3PbI_{3-x}Br_x$ and $CH_3NH_3PbI_{3-x}Cl_x$ have been investigated to improve the properties of resistive switching memory.[25,28] Due to the lower formation activation energy and migration activation energy of bromide vacancies ($V_{Br}^{\cdot}$), the increase in Br content of $CH_3NH_3PbI_{3-x}Br_x$ decreases the onset voltage of the device.[25] The precise resistive switching mechanism of the hybrid perovskite materials depends on their electrode materials. Inert electrode materials such as Au and Pt in contact with the perovskite layer only provide the transport path for charge carriers. Therefore, the intrinsic defects such as iodine interstitials and vacancies cause the resistive switching behavior.[25,27] However, reactive metals such as Ag and Cu can form the second phase such as AgI and be doped into the perovskite near the electrode/perovskite junction.[32] These reactive ions transport under electric field and dominantly contribute to the resistive switching behavior of the hybrid perovskite.[26,28]

An important factor that can influence the carrier transport and defect migration of the halide perovskite film is the $CH_3NH_3PbI_3$ – electrode interface. The TiO_2 - $CH_3NH_3PbI_3$ interface affects the power conversion efficiency of the perovskite solar cells due to the capacitive effect, charge trapping, and ion accumulation at the TiO_2 - $CH_3NH_3PbI_3$ interface.[23] Interface trap states cause the accumulation of electric and ionic charges. This space charge, in turn, inhibits electrons extraction from the perovskite to TiO_2.[33-35] However, the effect of the interface on the carrier transport of ReRAM devices has not been systematically studied.

Herein, we study how the interface between the hybrid perovskite and oxide layers affects the transport of charge carriers and point defects by comparing two different multilayer films (Au/$CH_3NH_3PbI_3$/TiO_2/F doped SnO_2 (FTO) and Au/$CH_3NH_3PbI_3$/ FTO). The inert Au was used as a top electrode to prevent electrochemical reaction with perovskite layer from the Au electrode. It is found that an addition of TiO_2 layer between CH_3NH_3PbI and FTO increased Schottky junction barrier height at the interface when the negative bias is applied to the Au electrode. Strong electrostatic attraction between I_i' and $V_O^{\cdot\cdot}$ caused the larger space charge polarization and higher on/off ration (10^3), and reliable retention time, over 10^4 seconds in the Au/$CH_3NH_3PbI_3$/TiO_2/FTO structure. The space charge of ions which are electrically bound to the TiO_2 – perovskite interface leads to a very asymmetric I-V curves.

Results and Discussion

The device schematic of the Au/$CH_3NH_3PbI_3$/TiO_2/FTO structure are shown in Figures 1a. A cross-sectional SEM image of 200 nm thick $CH_3NH_3PbI_3$ perovskite film deposited on TiO_2 (20 nm)/FTO substrate is also shown in Figure 1b. The $CH_3NH_3PbI_3$ perovskite layer was uniformly crystallized on the TiO_2 layer without pin-holes. Figure 1c shows that the perovskite layer

consists of grains with the size of 325 nm on average. XRD patterns of the $CH_3NH_3PbI_3/TiO_2/FTO$ structure in Figure 1d exhibit strong peaks of the perovskite phase at 14.1°, 28.5°, and 31.9°, which are assigned to the tetragonal structure of (110), (220), and (312) planes. No impurity peaks were observed from the formation of the perovskite structure on the TiO_2/FTO substrate. Each main peak of anatase and rutile TiO_2 from the standard spectrum exhibits at 25.28° (JCPDS no.:21-1272 for anatase) and 27.45° (JCPDS no.: 21-1276 for rutile), respectively. However, diffraction peaks of TiO_2 were not observed from the TiO_2/FTO substrate, suggesting that low temperature ALD deposition of TiO_2 results in an amorphous structure.[36-38]

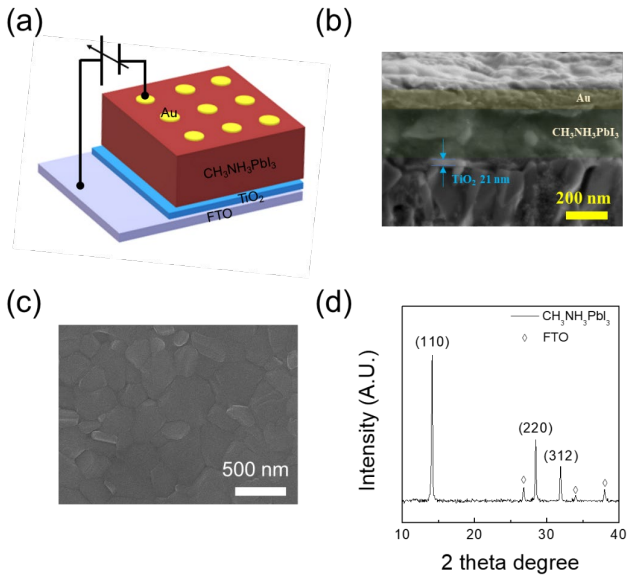

Figure 1. (a) A schematic of the device structure: Au (top electrode)/$CH_3NH_3PbI_3/TiO_2$/FTO (bottom electrode), (b) cross-sectional and (c) plan SEM images of the device, (d) XRD patterns of the $CH_3NH_3PbI_3$ layer fabricated on the TiO_2/FTO substrate.

Figure 2a and 2b show I-V curves of $Au/CH_3NH_3PbI_3$/FTO and $Au/CH_3NH_3PbI_3/TiO_2$/FTO. The insertion of TiO_2 layer results in a very asymmetric switching behavior. For I-V curve measurement, electric bias with a sequence of 0 V → 2 V → 0 V → −2

V → 0 V was applied to the Au electrode. During the I-V curve measurement, the FTO substrate was grounded. As the voltage sweeps from 0 V to 2 V, a sudden increase in current is found at 0.85 V. This process is called a "SET" process, as the resistance state of the device changes from an initial high resistance state (HRS) to a low resistance state (LRS). After the device turned to LRS, electric current remains. At V = -1.4 V, the resistance state switches to a high resistance state (HRS), which is called "RESET" process. On the other hand, the Au/$CH_3NH_3PbI_3$/FTO device exhibits a more symmetric I-V curve with the set voltage at 1.4 V and the reset voltage at -1.1 V. Since the Au/$CH_3NH_3PbI_3$/FTO structure does not have a TiO_2 layer, it has lower resistance than the Au/$CH_3NH_3PbI_3$/TiO_2/FTO structure in HRS.

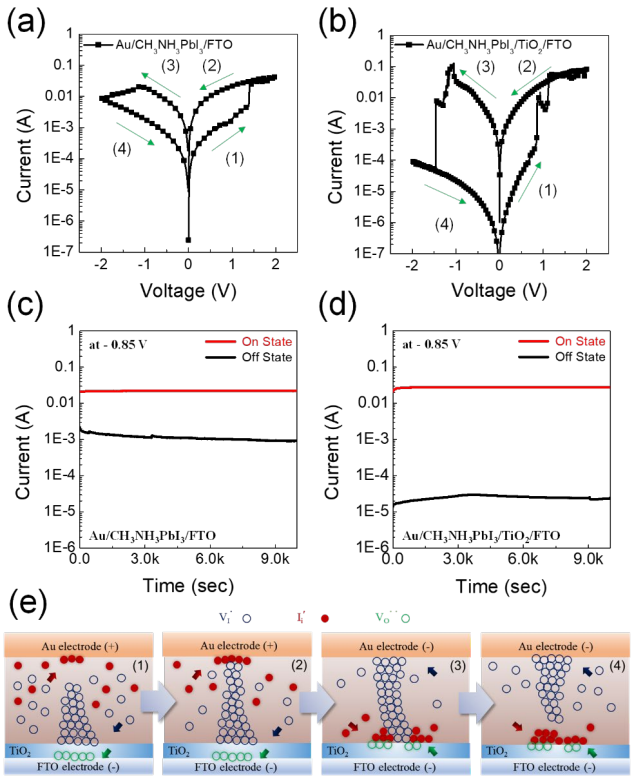

Figure 2. I–V curves of (a) Au/$CH_3NH_3PbI_3$/FTO and (b) Au/$CH_3NH_3PbI_3$/TiO_2/FTO devices and (c) and (d) are their retention characteristics at LRS and HRS. Schematic diagrams corresponding to stages (1) – (4) in Figure 2(b) are (e-1), (e-2), (e-3), and (e-4).

Table 1. I(LRS)/I(HRS) values of Au/$CH_3NH_3PbI_3$/FTO and Au/$CH_3NH_3PbI_3$/TiO_2/FTO at 0.85 V and -0.85 V.

	I(LRS)/I(HRS) at 0.85 V	**I(LRS)/I(HRS) at -0.85 V**
Au/$CH_3NH_3PbI_3$/FTO	13.27	11.13
Au/$CH_3NH_3PbI_3$/TiO_2/FTO	31.43	1530.71

Table 1 shows I(LRS)/ I(HRS) of Au/$CH_3NH_3PbI_3$/FTO and Au/$CH_3NH_3PbI_3$/TiO_2/FTO at 0.85V and -0.85V, which quantifies the asymmetry of the Au/$CH_3NH_3PbI_3$/TiO_2/FTO structure. It is noted that I(LRS)/I(HRS) is the largest when the negative bias is applied to Au/$CH_3NH_3PbI_3$/TiO_2/FTO. Figure 2c and Figure 2d show the retention performance of two devices, which is another good performance indicator of the ReRAM device.[39] The test for both devices were conducted at -0.85 V of LRS and HRS. They presented unchanged values of LRS and HRS over a period of 10^4 s. This is comparable to a recent result which reported an organic-inorganic perovskite memory device with a retention time over 10^4 s, which exhibits a good stability of the device.[25, 27-28, 37, 40] I-V and retention characteristics in Figure 2 suggest that the interface between $CH_3NH_3PbI_3$ and TiO_2 influences on the resistive switching mechanism. As a result, the Au/$CH_3NH_3PbI_3$/TiO_2/FTO structure exhibits a more asymmetric resistive behavior.

Additional cyclic measurements were performed in Figure 3a and 3b and both devices showed good endurance stability until 350 subsequent I-V sweeps. The first and the subsequent cycle showed the same V_{SET} and V_{RESET} in both devices without electroforming process as shown in Figure S1.[41] This is because high defects ($V_I^{\cdot}$) and (I_i') concentrations, which are ~5 × 10^{20} cm^{-3} ($V_I^{\cdot}$) and ~5 × 10^{16} cm^{-3} (I_i'),[42] in the $CH_3NH_3PbI_3$ layer can form a conductive path at

low voltage. Moreover, 50 devices of Au/$CH_3NH_3PbI_3$/FTO and Au/$CH_3NH_3PbI_3$/TiO_2/FTO structure were measured to examine the reproducibility of working cells. Set voltage (V_{SET}) and reset voltage (V_{RESET}) of these 50 devices are shown in Figure 3c and 3d. The variation of the performance is small. These results indicate that the devices can be potentially utilized in nonvolatile memory applications.

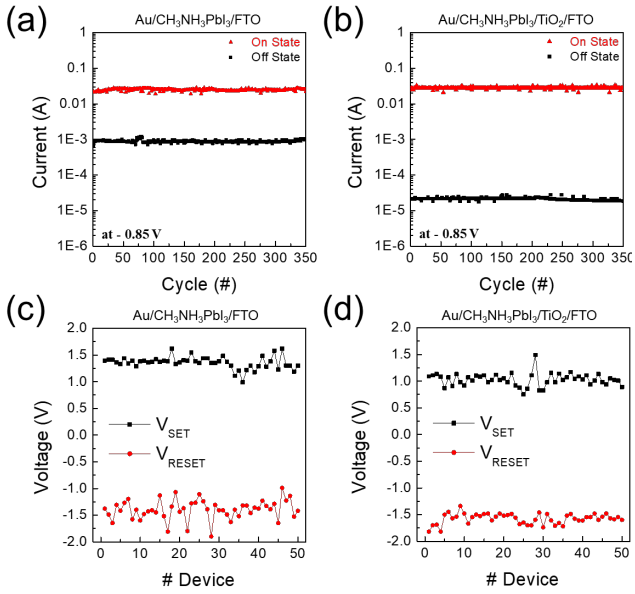

Figure 3. I–V curves of (a) Au/$CH_3NH_3PbI_3$/FTO and (b) Au/$CH_3NH_3PbI_3$/TiO_2/FTO devices through 350 successive cycles. (c) and (d) are their probability distribution for 50 different devices.

The physical origin of the asymmetric I-V curve is related to how defects are accumulated at different interfaces. The switching mechanism of the halide perovskite is explained by the formation and rupture of the defect chains.[25-28] Out of several vacancies (V_i, V_{MA}, V_{Pb}), interstitials (Pb_i, MA_i, I_i), and antisites (Pb_i, I_{Pb}), V_I has the low formation energy and the highest defect concentration. In addition, the migration energy of I_i (0.15 eV) and V_I (0.25 eV) is much lower than that of Pb^{2+} (0.84 eV) and $CH_3NH_3^+$ (2.31 eV) in the $CH_3NH_3PbI_3$ layer.[42-44] Therefore, abundant and mobile $V_I^{\cdot}$ and I_i' defects set a conductive pathway under

external bias and the perovskite layer turns from HRS to LRS. The conduction mechanism of the film has been described with hopping of injected electrons.[45, 46] It is because $V_I^{\cdot}$ defects play a role of trap sites in the $CH_3NH_3PbI_3$ layer below the conduction band of $CH_3NH_3PbI_3$. Once the mobile $V_I^{\cdot}$ defects form a continuous chain, $V_I^{\cdot}$ provides a conductive path for the injected electrons. Trap-to-trap hopping of electrons at nearby $V_I^{\cdot}$ defect sites turn the perovskite layer to LRS. To reset the film from LRS to HRS, an opposite electric to rupture the conduction path. Figure 2e schematically explains the migration and alignment of defects and Figures 2(e-1) – 2(e-4) correspond to the stage (1) – (4) of I-V curve of Au/$CH_3NH_3PbI_3$/TiO_2/FTO in Figure 2(b). A main difference between Figure 2(e-2) and 2(e-4) is that the interstitial defects in the perovskite layer can make a strong bond with TiO_2 in Fig. 2(e-4), since positively charged oxygen vacancies in TiO_2 can drift under DC bias.[47] However, Au/$CH_3NH_3PbI_3$/FTO device shows similar interstitials defect alignment at the Au - $CH_3NH_3PbI_3$ interface and $CH_3NH_3PbI_3$ – FTO interface shown in Figure S2 (2) and (4). This is because interstitials defects have the same bond strength with Au and FTO under DC bias.

When the negative bias is applied to Au, the oxygen vacancies move toward the $CH_3NH_3PbI_3$ - TiO_2 interface and hold the negatively charged iodine interstitials. In comparison to the $CH_3NH_3PbI_3$ - Au interface [Fig. 2(e-2)], more $I_i^{\prime}$ are accumulated at the $CH_3NH_3PbI_3$ - TiO_2 interface [Fig. 2(e-4)] due to the strong electric affinity between negatively charged $I_i^{\prime}$ and positively charge $V_O^{\cdot\cdot}$. This $I_i^{\prime}$ accumulation layer at the $CH_3NH_3PbI_3$ - TiO_2 interface can produce space charge and increase the barrier height at the $CH_3NH_3PbI_3$ - TiO_2 interface. In contrast, when the positive bias is applied to Au, the most abundant $V_I^{\cdot}$ mainly forms the chain and the most mobile $I_i^{\prime}$ moves toward the Au electrode. Since the perovskite - Au interface is Ohmic and there is no strong electrostatic attraction between $I_i^{\prime}$ and Au, a part of $I_i^{\prime}$ near Au does

not have a large impact on the resistance. The space charge effect at the $CH_3NH_3PbI_3$-TiO_2 interface also explains why I-V curve of Au/$CH_3NH_3PbI_3$/FTO is much more symmetric than that of Au/$CH_3NH_3PbI_3$/TiO_2/FTO. In a case of Au/$CH_3NH_3PbI_3$/FTO, the high electron concentration of FTO shields $V_O^{\cdot\cdot}$ and the migration of $V_O^{\cdot\cdot}$ under the bias is not significant in FTO. Hence, I_i' may not be strongly bound to the $CH_3NH_3PbI_3$ - FTO and the space charge is not large enough to produce the very asymmetric I-V curve.

To further verify the effect of the ion accumulation on the energy barrier at the $CH_3NH_3PbI_3$-TiO_2, $CH_3NH_3PbI_3$-FTO, and $CH_3NH_3PbI_3$-Au interfaces on the electron transport, the unipolar resistive switching behavior is also measured at the compliance current of 100 mA. Figures 4a - 4d show I-V curves of Au/$CH_3NH_3PbI_3$/FTO and Au/$CH_3NH_3PbI_3$/TiO_2/FTO without flipping the polarity of external bias. Samples were not exposed to electric field before this measurement. When the Au electrode is positively biased, characteristics of I-V curves of Au/$CH_3NH_3PbI_3$/FTO and Au/$CH_3NH_3PbI_3$/TiO_2/FTO are similar, as shown in Figure 4a and 4c. The switching from HRS to LRS occurs only for the first sweep. Once the samples reach the LRS, subsequent unipolar sweep does not make samples return to the HRS. When the Au is negatively biased, different switching behaviors are observed in Figure 4b and 4d. Au/$CH_3NH_3PbI_3$/FTO switches from the HRS to the LRS during the first voltage sweep and stays in the LRS during subsequent sweeps (Fig. 4b). However, the application of the negative bias does not change Au/$CH_3NH_3PbI_3$/TiO_2/FTO from the HRS to the LRS (Fig. 4d). The Au/$CH_3NH_3PbI_3$/TiO_2/FTO maintains the HRS, though it is exposed to multiple unipolar sweeps of the negative bias. In Figure 4d, it is also noted that the resistance of Au/$CH_3NH_3PbI_3$/TiO_2/FTO in the HRS is much larger than that of Au/$CH_3NH_3PbI_3$/FTO in the HRS. This suggests that the mobile ions (mainly I_i') interact with $CH_3NH_3PbI_3$/TiO_2 and

$CH_3NH_3PbI_3$/FTO very differently when the negative bias is applied to the Au electrode. Due to the migration of $V_O^{\cdot\cdot}$ in TiO_2 under electric field, Schottky junction barrier of I_i' can be formed at $CH_3NH_3PbI_3$/ TiO_2 interface, as schematically explained in Figure 4e.[48] The accumulated charge layer suppresses the electron transport from $CH_3NH_3PbI_3$ to TiO_2 charges transport and prevents the formation of the conductive V_I channels.

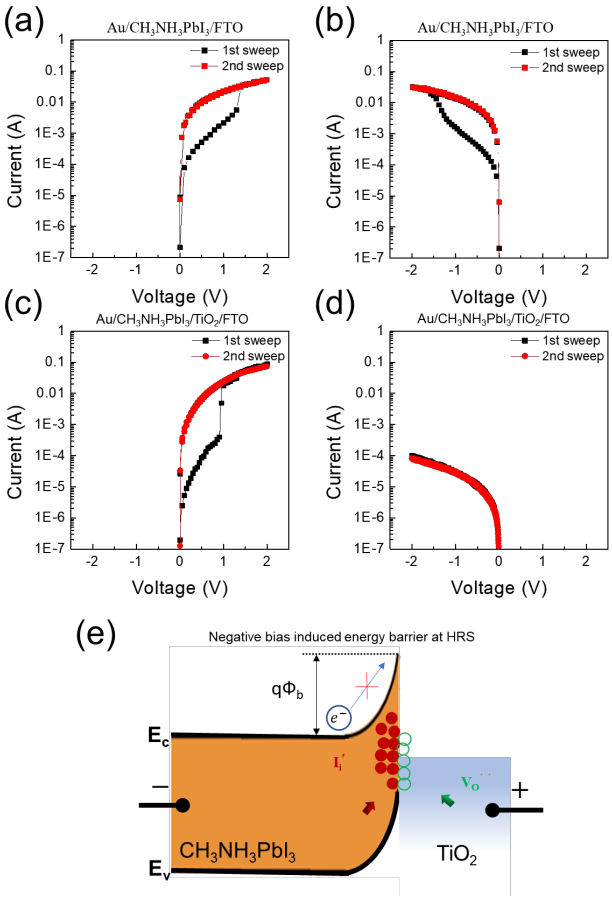

Figure 4. (a), (b) unipolar I–V curves of Au/$CH_3NH_3PbI_3$/FTO ((a) positive bias is applied to Au, (b) negative bias is applied to Au); (c), (d) unipolar I–V curves of Au/$CH_3NH_3PbI_3$/TiO_2/FTO ((c) positive bias is applied to Au, (d) negative bias is applied to Au); (e) a schematic on the band bending at the $CH_3NH_3PbI_3$/TiO_2 interface under negative bias applied to Au.

An additional evidence to support that Schottky junction at the interface is modified by addition of TiO_2 is provided by inserting the phenly-61C-butyric acid methyl ester (PCBM) layer between the perovskite and FTO layers. TiO_2 and PCBM have a similar function to passivate the surface of the perovskite layer. However, while the dielectric TiO_2 layer holds charged defects on the surface under E-field, the conductive PCBM layer does not provide any additional charge storage function.[45-47] Figure S3 shows no resistive switching behavior of the Au/ $CH_3NH_3PbI_3$/PCBM/FTO device. This result indicates that a strong electrostatic attraction between negatively charged I_i' and positively charge $V_O^{\cdot\cdot}$ under DC bias at the $CH_3NH_3PbI_3/TiO_2$ interface contributes to a unique switching behavior of Au/perovskite/TiO_2/FTO device.

The space charge at the $CH_3NH_3PbI_3$-TiO_2 interface was examined by measuring the capacitance of the films as a function of the frequency. During the measurement, the external DC bias ranging from -1.5V to 1.5V was also applied. Figure 5 shows the capacitance-frequency (C-f) curves of Au/$CH_3NH_3PbI_3$/FTO and Au/$CH_3NH_3PbI_3/TiO_2$/FTO. Large capacitance at the frequency below 10^3 Hz is due to space charge polarizations resulting from the charge imbalance at different interfaces, while the electronic and ionic polarization mechanism is responsible for the capacitance at high frequency.[33]

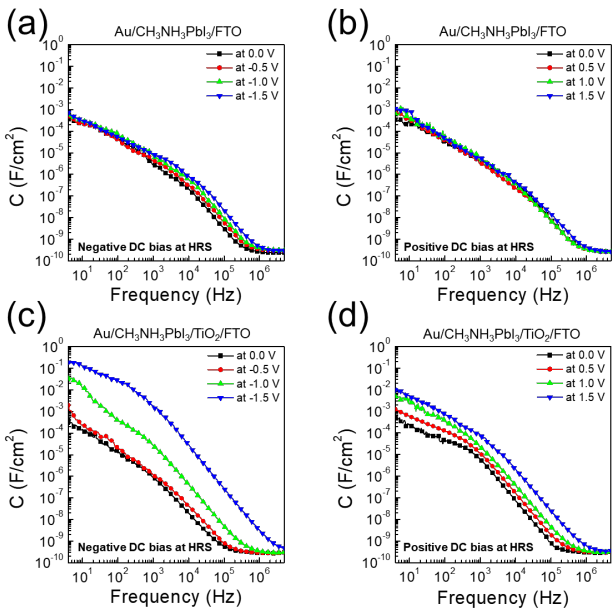

Figure 5. Capacitance-frequency (C-f) curves of Au/$CH_3NH_3PbI_3$/FTO [(a) the negative DC bias to Au, (b) the positive DC bias to Au] and Au/$CH_3NH_3PbI_3$/TiO_2/FTO [(c) the negative DC bias to Au, (d) the positive DC bias to Au].

In Figures 5a and 5b, C-f curves of Au/$CH_3NH_3PbI_3$/FTO under different positive and negative bias are similar. This suggests that Au - $CH_3NH_3PbI_3$ interface and $CH_3NH_3PbI_3$ - FTO interface contribute similarly to the space charge polarization. However, C-f curves of Au/$CH_3NH_3PbI_3$/TiO_2/FTO in Figure 5c and 5d exhibit the significant effect of external bias on the capacitance. This indicates that the TiO_2 layer increases the space charge polarization and the effect of TiO_2 on the capacitance has the polarity. When the negative bias is applied to Au, an increase in the absolute bias increases the capacitance. The accumulation of the negatively charged iodine interstitials at the $CH_3NH_3PbI_3$ - TiO_2 interface dramatically increases the space charge polarization. This is attributed to the migration of $V_O^{\cdot\cdot}$ in TiO_2 under DC bias.[49] Larger negative bias applied to Au increases more migration of $V_O^{\cdot\cdot}$ to the TiO_2-$CH_3NH_3PbI_3$ interface and hold more I_i' by the electrostatic attraction. The accumulated I_i' increases the space charge

polarization of the film. The C-V curves support that the electrostatic force causes the accumulation of I_i' at the $CH_3NH_3PbI_3$ - TiO_2 interface if the negative bias (or positive bias) is applied to Au (or FTO) rather than forming the defect chain. These accumulated defects which work as Schottky barrier shows why the resistance of the Au/$CH_3NH_3PbI_3$/TiO_2/FTO at HRS has the dependence on the direction of the external electric field.

Conclusion

In summary, we systematically studied how the $CH_3NH_3PbI_3$ - TiO_2 interface asymmetrically influences the resistive switching of the Au/$CH_3NH_3PbI_3$/TiO_2/FTO device by changing the formation and rupture of defect chains. When negative bias is applied to the Au electrode, iodine interstitials with the lowest migration energy moves in $CH_3NH_3PbI_3$ toward TiO_2 and pile up at the $CH_3NH_3PbI_3$ - TiO_2 interface. Under the same condition, oxygen vacancies in TiO_2 layer also travel to the $CH_3NH_3PbI_3$ - TiO_2 interface, strongly attract iodine interstitials, and form Schottky barrier at the $CH_3NH_3PbI_3$ - TiO_2 interface. Consequently, the modified Schottky junction barrier of the Au/$CH_3NH_3PbI_3$/TiO_2/FTO device reduces electric current at HRS when negative electric bias is applied to Au. This leads to the higher on/off ratio, 10^3 and good retention time, $> 10^4$ seconds during the resistive switching. Our study shows that the interface in contact with the halide perovskite layer can control the appearance of the conductive chains and the bipolar resistive switching behavior in the halide perovskite film.

Experimental Section

Preparation of TiO_2 film coated substrates. Before depositing the hybrid perovskite layer, a half of FTO coated glasses (TEC15 from Pilkington) were coated with dense 20 nm thick

TiO_2 film using an atomic layer deposition (ALD) system. FTO coated glasses were cut and then sequentially cleaned by acetone, deionized (DI) water, and ethanol for 15 min, respectively. Tetrakis(dimethylamido)titanium (TDMAT) as a precursor was heated at 75 °C for a sufficient vapor pressure. The temperature in the reaction chamber was kept at 60 °C for the deposition with the processing pressure ~ 0.2 Torr. High-purity N2 (flow rate, 20 sccm) was used as the carrier and purging gas. The set-up program was as follows: 150 ms pulse of TDMAT, 10 s purge of N_2, 500 ms pulse of H_2O, and 15 s purge of N_2 for every full cycle. TiO_2 layer was grown with a deposition rate of 0.05 nm/cycle.

Fabrication of the device. Au/$CH_3NH_3PbI_3$/TiO_2/FTO or Au/$CH_3NH_3PbI_3$/FTO structures were fabricated on TiO_2/FTO/glass or FTO/glass substrates. A perovskite ($CH_3NH_3PbI_3$) precursor was prepared by an adduct method, as reported previously.[50] Lead iodide (PbI_2), methyl ammonium iodide (MAI, CH_3NH_3I), and dimethyl sulfoxide (DMSO) with a molar ratio of 1:1:1 are dissolved in N,N-dimethylformamide (DMF) and then stirred for 45 min. This liquid solution was spin-coated on top of the TiO_2/FTO at 4000 rpm for 25 s, and after 10 s, 0.5 ml of diethyl ether was rapidly dropped onto the substrates. The spin-coated samples were annealed at 60 °C and 100 °C for 3 and 10 min, respectively. Finally, a 60 nm-thick Au electrode was deposited on the shadow-masked perovskite film by the e-beam evaporation.

Characterization. The crystallographic information of deposited films was obtained by X-ray diffraction (XRD; X'Pert, PANalytical). The surface morphology and cross-sectional view of the devices were examined using a field-emission scanning electron microscope (FESEM; XL-30F, FEI). Current-voltage characterization and retention performance were measured by a probe station at room temperature. An external bias was applied to the top Au electrode with the FTO bottom electrode grounded in a voltage sequence of 0 V → 2 V → 0 V → −2 V → 0 V.

ASSOCIATED CONTENT

Supporting Information.

The Supporting Information is available free charge of at *http://pubs.acs.org/*

Full I-V curves of both Au/$CH_3NH_3PbI_3$/FTO and Au/$CH_3NH_3PbI_3$/TiO_2/FTO devices for the first 50 cycles; Schematic diagram corresponding to the stages of (1) – (4) in Figure 2 (a); I-V curve of the Au/$CH_3NH_3PbI_3$/PCBM/FTO device. (file type, i.e., PDF)

AUTHOR INFORMATION

Corresponding Author

Jung-Kun Lee - *Department of Mechanical Engineering & Materials Science, University of Pittsburgh, Pennsylvania 15261, USA;* orcid.org/0000-0002-7778-7679; E-mail: jul37@pitt.edu

Authors

Seongha Lee - *Department of Mechanical Engineering & Materials Science, University of Pittsburgh, Pennsylvania 15261, USA*

Sarah Wolfe - *Department of Mechanical Engineering & Materials Science, University of Pittsburgh, Pennsylvania 15261, USA*

Jorge Torres - *Department of Electrical and Computer Engineering, University of Pittsburgh, Pennsylvania 15261, USA*

Minhee Yun - *Department of Electrical and Computer Engineering, University of Pittsburgh, Pennsylvania 15261, USA;* orcid.org/0000-0002-6445-6280

Complete contact information is available at *https://pubs.acs.org/*

Funding Sources

J.-K.L. received funding from National Science Foundation, USA (NSF 1709307), Korea Institute of Energy Technology Evaluation and Planning (KETEP) grant funded by the Korea government (MOTIE) (20193091010460).

Notes

The authors declare no competing financial interest.

ACKNOWLEDGMENT

This work was supported by National Science Foundation, USA (NSF 1709307), Korea Institute of Energy Technology Evaluation and Planning (KETEP) grant funded by the Korea government (MOTIE) (20193091010460).

REFERENCES

(1) Waser, R.; Aono, M. Nanoionics-Based Resistive Switching Memories. *Nat. Mater.* **2007**, 6, 833–840.

(2) Goux, L.; Valov, I. Electrochemical Processes and Device Improvement in Conductive Bridge RAM Cells. *Phys. Status Solidi A.* **2016**, 213, 274-288.

(3) Waser, R.; Dittmann, R.; Staikov, G.; Szot, K. Redox-Based Resistive Switching Memories-Nanoionic Nechanisms, prospects, and challenges. *Adv. Mater.* **2009,** 21, 2632–2663.

(4) Privitera, S.; Bersuker, G.; Lombardo, S.; Bongiorno, C; Gilmer, D. C. Conductive Filament Structure in HfO_2 Resistive Switching Memory. *Solid-State Electron.* **2015,** 111, 161-165.

(5) Li, Y.; Long, S.; Liu, Q.; Lv, H.; Liu, M. Resistive Switching Performance Improvement via Modulating Nanoscale Conductive Filament, Involving the Application of Two-Dimensional Layered Materials. *Small* **2017,** 13, No. 1604306.

(6) Valov, I.; Kozicki, M. N. Cation-Based Resistance Change Memory. *J. Phys. D: Appl. Phys.* **2013,** 46, No. 074005.

(7) Valov, I.; Tsuruoka, T. Effects of Moisture and Redox Reactions in VCM and ECM Resistive Switching Memories. *J. Phys. D: Appl. Phys.* **2018,** 51, No. 413001.

(8) Zhao, L.; Chen, H. -Y.; Wu, S. -C.; Jiang, Z.; Yu, S.; Hou, T. -H.; Wong, H. -S. P.; Nishi, Y. Multi-Level Control of Conductive Nano-Filament Evolution HfO_2 ReRAM by Pulse-Train Operations. *Nanoscale* **2014,** 6, 5698-5702.

(9) Lee, D.; Woo, J.; Park, S.; Cha, E.; Lee, S.; Hwang, H. Dependence of Reactive Metal Layer on Resistive Switching in a Bi-layer Structure Ta/HfOx Filament Type Resistive Random Access Memory. *Appl. Phys. Lett.* **2014,** 104, No. 083507.

(10) Song, S. J.; Seok, J, Y.; Yoon, J. H.; Kim, K. M.; Kim, G. H.; Lee, M. H.; Hwang, C. S. Real-Time Identification of the Evolution of Conducting Nano-Filament in TiO_2 Thin Film ReRAM. *Sci. Rep.* **2013,** 3, No. 3443.

(11) Burschka, J.; Pellet, N.; Moon, S. J.; Humphry-Baker, R.; Gao, P.; Nazeeruddin, M. K.; Grätzel, M. Sequential Deposition as a Route to High-Performance Perovskite-Sensitized Solar Cells. *Nature* **2013,** 499, 316−319.

(12) Filip, M. R.; Eperon, G. E.; Snaith, H. J.; Giustino, F., Steric Engineering of Metal-Halide Perovskite with Tunable Optical Band Gaps. *Nat. Commun.* **2014,** 5, No. 5757.

(13) Lee, M. M.; Teuscher, J.; Miyasaka, T.; Murakami, T. N.; Snaith, H. J. Efficient Hybrid Solar Cells Based on Meso-Superstructured Organometal Halide Perovskites. *Science* **2012,** 338, 643−647.

(14) Kojima, A.; Teshima, K.; Shirai, Y.; Miyasaka, T. OrganoMetal Halide Perovskite as Visible-Light Sensitizers for Photovoltaic Cells. *J.Am. Chem. Soc.* **2009,** 131, 6050–6051.

(15) Leblebici, S. Y.; Leppert, L.; Li, Y.; Reyes-Lillo, S. E.; Wickenburg, S.; Wong, E.; Lee, J.; Melli, M.; Ziegler, D.; Angell, D. K. Ogletree, D. F.; Ashby, P. D.; Toma, F. M.; Neaton, J. B.; Sharp, I. D.; Weber-Bargioni, A. Facet-Dependent Photovoltaic Efficiency Variations in Single Grains of Hybrid Halide Perovskite. *Nat. Energy* **2016,** 1, No. 16093.

(16) Lee, S. Roh, H. -S., Han, G. S.; Lee, J. -K. Controlled Oxidation of Ni for Stress-Free Hole Transport Layer for Large-Scale Perovskite Solar Cell. *Nano Res.* **2019,** 12, 3098-3094.

(17) Tan, Z. –K.; Moghaddam, R. S.; Lai, M. L.; Docampo, P.; Higler, R.; Deschler, F.; Price, M.; Sadhanala, A.; Pazos, L. M.; Credgington, D.; Hanusch F.; Bein, T.; Snaith, H. J.; Friend, R. H. Bright Light-Emitting Diodes Based on Organometal Halide Perovskite. *Nat. Nanotech.* **2014,** 9, 687–692.

(18) Kim, Y. –H.; Cho, H.; Heo, J. H.; Kim, T. -S.; Myoung. N.; Lee, C. -L.; Im, S. H.; Lee, T. -W. Multicolored Organic/Inorganic Hybrid Perovskite Light-Emitting Diodes. *Adv. Mater.* **2015,** 27, 1248–1254.

(19) Cho, H.; Jeong, S. -H.; Park, M. -H.; Kim, Y. -H.; Wolf, C.; Lee, C. -L., Heo, J. H.; Sadhanala, A.; Myoung, S.; Yoo, S.; Im, S. H.; Friend, R. H.; Lee, T. -W. Overcoming the Electroluminescence Efficiency Limitation of Perovskite Light-Emitting Diodes. *Science* **2015,** 350, 1222–1225.

(20) Senanayak, S. P.; Yang, B.; Thomas, T. H.; Giesbrecht, N.; Huang, W.; Gann, E.; Nair, B.; Goedel, K.; Guha, S.; Moya, X.; McNeill, C. R.; Docampo, P.; Sadhanala, A.; Friend, R. H.; Sirringhaus, H. Understanding Charge Transport in Lead Iodide Perovskite Thin-Film Field-Effect Transistors. *Sci. Adv.* **2017,** 3, No. 1601935.

(21) Lee, Y.; Kwon, J.; Hwang, E.; Ra, C. -H.; Yoo, W. J.; Ahn, J. -H.; Park, J. H.; Cho, J. H. High-Performance Perovskite-Graphene Hybrid Photodetector. *Adv. Mater.* **2015,** 27, 41–46.

(22) Zhu, H.; Fu, Y.; Meng, F.; Wu, X.; Gong, Z.; Ding, Q.; Gustafsson, M. V.; Trinh, M. T.; Jin, S.; Zhu. X. -Y. Lead Halide Perovskite Nanowire Lasers with Low Lasing Thresholds and High Quality Factors. *Nat. Mater.* **2015,** 15, 636-642.

(23) Chen, B.; Yang, M. J.; Priya, S.; Zhu, K. Origin of J−V Hysteresis in Perovskite Solar Cells. *J. Phys. Chem. Lett.* **2016,** 7, 905−917.

(24) Yuan, Y.; Huang, J. Ion Migration in Organometal Trihalide Perovskite and its Impact on Photovoltaic Efficiency and Stability. *Acc. Chem. Res.* **2016,** 49, 286−293.

(25) Hwang, B.; Gu, C.; Lee, D.; Lee, J. -S. Effect of Halide-Mixing on the Switching Behaviors of Organic-Inorganic Hybrid Perovskite Memory. *Sci Rep.* **2017,** 7, No. 43794.

(26) Sun, Y.; Tai, M.; Song, C.; Wang, Z.; Yin, J.; Li, F.; Wu, H.; Zeng, F.; Lin, H.; Pan, F. Competition between Metallic and Vacancy Defect Conductive Filaments in a $CH_3NH_3PbI_3$-Based Memory Device. *J. Phys. Chem. C* **2018,** 122, 6431−6436.

(27) Gu, C.; Lee, J. -S. Flexible Hybrid Organic-Inorganic Perovskite Memory. *ACS Nano* **2016,** 10, 5413−5418.

(28) Yoo, E.; Lyu, M.; Yun, J. -H.; Kang, C.; Choi, Y.; Wang, L. Bifunctional Resistive Switching Behavior in an Organolead Halide Perovskite Based Ag/$CH_3NH_3PbI_{3-x}Cl_x$/FTO structure. *J. Mater. Chem. C* **2016,** 4, 7824-7830.

(29) Zhu, X.; Lu, W. D. Optogenetics-Inspired Tunable Synaptic Functions Memristors. *ACS Nano* **2018,** 12, 1242-1249.

(30) Zhao, X.; Wang, Z.; Li, W.; Sun, S.; Xu, H.; Zhou, P.; Xu, J.; Lin, Y.; Liu, Y. Photoassisted Electroforming Method for Reliable Low-Power Organic-Inorganic Perovskite Memristors. *Adv. Funct. Mater.* **2020,** 30, No. 1910515.

(31) Yang, B.; Brown, C. C.; Huang, J.; Collins, L.; Sang, X.; Unocic, R. R.; Kalinin, S. V.; Belianinov, A.; Jakowski, J.; Geohegan, D. B. Enhancing Ion Migration in Grain Boundaries of Hybrid Organic-Inorganic Perovskite by Chlorine. Adv. Funct. Mater. **2017,** 27, No. 1700749.

(32) Kato, Y.; Ono, L, K.; Lee, M. V.; Wang, S.; Raga, S. R.; Qi, Y. Silver Iodide Formation in Methyl Ammonium Lead Iodide Perovskite Solar Cells with Silver Top Electrode. *Adv. Mater. Interfaces* **2015,** 2, No. 1500195.

(33) Kim, H. -S.; Jang, I. -H.; Ahn, N.; Choi, M.; Guerrero, A.; Bisquert, J.; Park, N. -G. Control of I-V Hysteresis in $CH_3NH_3PbI_3$ Perovskite Solar Cell. *J. Phys. Chem. Lett.* **2015,** 6, 4633−4639.

(34) Wojciechowski, K.; Stranks, S. D.; Abate, A.; Sadoughi, G.; Sadhanala, A.; Kopidakis, N.; Rumbles, G.; Li, C. -Z.; Friend, R. H.; Jen, A. K. -Y.; Snaith, H. J. Heterojunction Modification for Highly Efficient Organic-Inorganic Perovskite Solar Cells. *ACS Nano* **2014,** 8, 12701-12709.

(35) Yu, F.; Han, G. S.; Tu, Y. J.; Roh, H. -S.; Lee, J. -K. Electron Extraction Mechanism in Low Hysteresis Perovskite Solar Cells Using Single Crystal TiO2 Nanorods. *J. Sol. Energy* **2018,** 167, 251-257.

(36) Zardetto, V.; Giacomo, F. D.; Lifka, H.; Verheijen, M. A.; Weijtens, C. H. L.; Black, L. E.; Veenstra, S.; Kessels, W. M. M.; Andriessen, R.; Creatore, M. Surface Fluorination of ALD TiO_2 Electron Transport Layer for Efficient Planar Perovskite Solar Cells. *Adv. Mater. Interfaces* **2018,** 5, No. 1701456.

(37) Kim, T. W.; Uchida, S.; Kondo, T.; Segawa, H. Optimization of TiO_2 Compact Layer Formed by Atomic Layer Deposition for Efficient Perovskite Solar Cells. *Appl. Phys. Lett.* **2019,** 115, No. 203902.

(38) Kim, I. S.; Haasch, R. T.; Cao, D. H.; Farha, O. K.; Hupp, J. T.; Kanatzidis, M. G.; Martinson, A. B. F. Amorphous TiO_2 Compact Layers via ALD for Planar Halide Perovskite Photovoltaics. *ACS Appl. Mater. Interfaces* **2016,** 8, 24310−24314.

(39) J. J. Yang, D. B. Strukov and D. R. Stewart, Memristive Devices for Computing. *Nat. Nanotechnol.* **2013,** 8, 13-24.

(40) Lin, G.; Lin, Y.; Cui, R.; Huang, H.; Guo, X.; Li, C.; Dong. J.; Guo, X.; Sun, B. An Organic-Inorganic Hybrid Perovskite Logic Gate for Better Computing. *J. Mater. Chem. C* **2015,** 3, 10793-10798.

(41) Lee, S.; Kim, H.; Kim, D. H.; Kim, W. B.; Lee, J. M.; Choi, J.; Shin, H, Han, G. S.; Jang, H. W.; Jung, H. S. Tailored 2D/3D Halide Perovskite Heterointerface for Substantially Enhanced Endurance in Conducting Bridge Resistive Switching Memory. *ACS Appl. Mater. Interfaces* **2020,** 12, 17039−17045

(42) Ming, W.; Chen, S.; Du, M.-H. Chemical Instability Leads to Unusual Chemical-Potential-Independent Defect Formation and Diffusion in Perovskite Solar Cell Material $CH_3NH_3PbI_3$. *J. Mater. Chem. A* **2016,** 4, 16975–16981.

(43) Choi, J.; Park, S.; Lee, J.; Hong, K.; Kim, D. -H.; Moon, C. W.; Park, G. D.; Suh, J.; Hwang, J.; Kim, S. Y.; Jung, H. S.; Park, N. -G.; Han, S.; Nam, K. T.; Jang, H. W. Organolead Halide Perovskites for Low Operating Voltage Multilevel Resistive Switching. *Adv. Mater.* **2016,** 28, 6562–6567.

(44) Eames, C.; Frost, J. M.; Barnes, P. R.; O'regan, B. C.; Walsh, A.; Islam, M. S. Ionic Transport in Hybrid Lead Iodide Perovskite Solar Cells. *Nat. Commun.* **2015,** 6, No. 7497.

(45) Wei, Z.; Eriguchi, K. Analytic Modeling for Nanoscale Resistive Filament Variation in ReRAM with Stochastic Differential Equation. *IEEE TRANSACTIONS ON ELECTRON DEVICES* **2017,** 64, 2201-2206.

(46) Wang, C.; Wu, H.; Gao, B.; Zhang, T.; Yang, Y.; Qian, H. Conduction Mechanisms, Dynamics and Stability in ReRAMs. *Microelectronic Engineering* **2018,** 187–188, 121–133.

(47) O'Regan, B. C.; Barnes, P. R. F.; Li, X.; Law, C.; Palomares, E.; Marin-Beloqui, J. M. Optoelectronic Studies of Methylammonium Lead Iodide Perovskite Solar Cells with Mesoporous TiO_2: Separation of Electronic and Chemical Charge Storage, Understanding Two Recombination Lifetimes, and the Evolution of Band Offsets during J-V Hysteresis. *J. Am. Chem. Soc.* **2015,** 137, 5087−5099.

(48) Guan, X.; Hu, W.; Haque, M. A.; Wei, N.; Liu, Z.; Chen, A.; Wu, T. Light-Responsive Ion-Redistribution-Induced Resistive Switching in Hybrid Perovskite Schottky Junctions. *Adv. Funct. Mater.* **2018,** 28, No. 1704665.

(49) Zhang, F.; Ma, W.; Guo, H.; Zhao, Y.; Shan, X.; Jin, K.; Tian, H.; Zhao, Q.; Yu, D.; Lu, X.; Lu, G.; Meng, S. Interfacial Oxygen Vacancies as a Potential Cause of Hysteresis in Perovskite Solar Cells. *Chem. Mater.* **2016,** 28, 802−812.

(50) Ahn, N.; Son, D. Y.; Jang, I. H.; Kang, S. M.; Choi, M.; Park, N. G. Highly Reproducible Perovskite Solar Cells with Average Efficiency of 18.3% and Best Efficiency of 19.7% Fabricated via Lewis Base Adduct of Lead(II) Iodide. *J. Am. Chem. Soc.* **2015,** 137, 8696−8699.

TOC

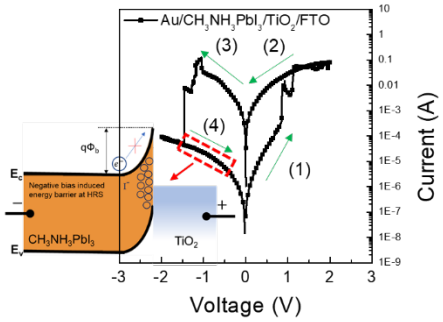
Au/CH3NH3PbI3/TiO2/FTO
(3)
(2)
(4)
(1)
qΦb
Ec
Ev
Negative bias induced energy barrier at HRS
I-
CH3NH3PbI3
TiO2
Current (A)
Voltage (V)